18F-Fluoride Signal Amplification Identifies Microcalcifications Associated With Atherosclerotic Plaque Instability in Positron Emission Tomography/Computed Tomography Images

^{18}F-fluoride signal amplification identifies microcalcifications associated with atherosclerotic plaque instability in PET/CT images

Short Title: PET imaging of atherosclerotic microcalcification

Michael D. Creager, BS,[1*] Tobias Hohl, BS,[1*] Joshua D. Hutcheson, PhD,[2*] Alastair J. Moss, MD,[3] Florian Schlotter, MD,[1] Mark C. Blaser, PhD,[1] Mi-Ae Park, PhD,[4] Lang Ho Lee, PhD,[1] Sasha A. Singh, PhD,[1] Carlos J. Alcaide-Corral, BS,[3] Adriana A. S. Tavares, PhD,[3] David E. Newby, MD,[3] Marie F. Kijewski, ScD,[4] Masanori Aikawa, MD, PhD,[1,5] Marcelo Di Carli, MD,[4] Marc R. Dweck, MD, PhD,[3] and Elena Aikawa, MD, PhD[1,5]

[1] Center for Interdisciplinary Cardiovascular Sciences, Division of Cardiovascular Medicine, Brigham and Women's Hospital, Harvard Medical School, Boston, MA, USA

[2] Florida International University, Miami, FL, USA

[3] British Heart Foundation, Centre for Cardiovascular Science, University of Edinburgh, Edinburgh, UK

[4] Division of Cardiovascular Medicine, Brigham and Women's Hospital, Harvard Medical School, Boston, MA, USA

[5] Center for Excellence in Vascular Biology, Division of Cardiovascular Medicine, Brigham and Women's Hospital, Harvard Medical School, Boston, MA, USA

* These authors contributed equally to this work

Journal Subject Terms: Imaging; Computerized Tomography (CT); Nuclear Cardiology and PET; Atherosclerosis

Corresponding author: Elena Aikawa, M.D., PhD
Brigham and Women's Hospital, Harvard Medical School
3 Blackfan St, 17th Floor, Room 1737, Boston, MA 02115
Phone: 617 730-7755
Email: eaikawa@bwh.harvard.edu

Total word count: 6,9001

ABSTRACT

Background: Microcalcifications in atherosclerotic plaques are destabilizing, predict adverse cardiovascular events, and are associated with increased morbidity and mortality. ^{18}F-fluoride PET/CT imaging has demonstrated promise as a useful clinical diagnostic tool in identifying high risk plaques; however, there is confusion as to the underlying mechanism of signal amplification seen in PET-positive, CT-negative image regions. This study tested the hypothesis that ^{18}F-fluoride PET/CT can identify early microcalcifications.

Methods and Results: ^{18}F-fluoride signal amplification derived from microcalcifications was validated against near infrared fluorescence (NIRF) molecular imaging and histology using an *in vitro* 3D hydrogel collagen platform, *ex vivo* human specimens, and a mouse model of atherosclerosis. Microcalcification size correlated inversely with collagen concentration. The ^{18}F-fluoride ligand bound to microcalcifications formed by calcifying vascular smooth muscle cell-derived extracellular vesicles in the *in vitro* 3D collagen system and exhibited an increasing signal with an increase in collagen concentration (0.25mg/ml collagen - $33.8x10^2 \pm 12.4x10^2$ CPM; 0.5 mg/ml collagen - $67.7x10^2 \pm 37.4x10^2$ CPM, $p=0.0014$), suggesting amplification of the PET signal by smaller microcalcifications. We further incubated human atherosclerotic endarterectomy specimens with clinically-relevant concentrations of ^{18}F-fluoride. The ^{18}F-fluoride ligand labeled microcalcifications in PET-positive, CT-negative regions of explanted human specimens as evidenced by ^{18}F-fluoride PET/CT imaging, NIRF and histological analysis. Additionally, the ^{18}F-fluoride ligand identified micro- and macrocalcifications in atherosclerotic aortas obtained from LDLr-deficient mice.

Conclusions: Our results suggest that ^{18}F-fluoride PET signal in PET-positive, CT-negative regions of human atherosclerotic plaques is the result of developing microcalcifications, and high surface area in regions of small microcalcifications may amplify PET signal.

Key words: Calcification; Microcalcification; Plaque rupture; Imaging: Imaging agent; PET/CT

CLINICAL PERSPECTIVE

Early microcalcification is associated with atherosclerotic plaque rupture in contrast to advanced later macrocalcification that potentially contributes to plaque stability. ^{18}F-fluoride positron emission tomography (PET) is believed to identify these regions of microcalcification. The objective of this manuscript was to evaluate the mechanism of ^{18}F-fluoride binding in atherosclerotic plaque using an *in vitro* microcalcification model and *ex vivo* human tissue, and to confirm feasibility for identification of atherosclerotic plaques with microcalcifications in an *in vivo* mouse model. ^{18}F-fluoride preferentially bound to the surface of nanocrystalline hydroxyapatite in regions that were remote from macrocalcific deposits. Moreover, the intensity of the ^{18}F-fluoride signal increased with smaller sized crystals of hydroxyapatite and was associated with histological markers of osteogenic activity. These novel mechanistic insights support ^{18}F-fluoride PET as a marker of microcalcification and a means of identifying coronary and carotid plaques with an adverse morphology. Clinical trials are ongoing to assess the prognostic utility of ^{18}F-fluoride PET imaging in patients at high risk of recurrent plaque rupture events.

INTRODUCTION

Coronary artery calcium is a common feature of atherosclerosis, and quantification of coronary artery calcium from computed tomographic scans predicts adverse coronary heart disease events [1-3]. Coronary artery calcification is a pathophysiologic process that is intrinsic to the atherosclerotic plaque and is triggered by inflammation as calcifying extracellular vesicles (EVs) are released from macrophages and vascular smooth muscle cells[4-7]. Large calcifications within the plaque form from microcalcifications, and microcalcifications result from the aggregation and fusion of individual calcifying EVs[6, 8]. Whereas large calcifications may provide biomechanical stability, microcalcifications (< 50 μm) that form within the fibrous cap intensify the incident stresses and can lead to microfractures and plaque rupture [9-19]. Indeed, microcalcification is apparent in high-risk atheroma, predicts adverse cardiovascular events, and is associated with increased morbidity and mortality[4, 13, 17, 20-26].

Computed tomography (CT) used in clinical applications has a resolution limit of approximately 200 μm, and therefore is not conducive to detecting microcalcifications[18, 19, 27-31]. Other imaging methods, such as intravascular ultrasound and optical coherence tomography, with resolution thresholds of 100 and 10 μm, respectively, can detect calcification but require invasive angiographic assessment[8, 32]. Therefore, noninvasive methods to identify microcalcification in atherosclerotic plaques are needed to detect high-risk patients and improve prevention and treatment of coronary artery disease[9, 13, 33-35].

^{18}F-fluoride positron emission tomography-computed tomography (PET/CT) is a sensitive and specific method for detecting microcalcification in high-risk atherosclerotic plaques *ex vivo,* despite relatively poor spatial resolution, is a highly reproducible technique for detection of early coronary artery calcification *in vivo*[4, 9, 21, 36-38]. Furthermore, the spatial resolution of ^{18}F-fluoride

PET/CT is adequate for localization to specific regions of atherosclerosis[9]; it has been shown to identify high-risk and ruptured coronary plaques in patients with coronary artery disease[32].

PET/CT imaging has been shown to detect vulnerable atherosclerotic plaques, and regions that are PET-positive distal and proximal to advanced macrocalcifications[9,24,37]. It has been suggested that the positive signal seen in these regions is due to developing microcalcifications surrounding macrocalcifications. These regions of microcalcifications have previously been associated with high-PET and low-CT signals. Because PET imaging has poorer resolution than CT imaging, the increased PET signal may be due to signal amplification resulting from increased surface area and, consequently, more binding sites, on microcalcifications compared to larger calcifications. It has been suggested that the CT-negative, PET-positive signal observed adjacent to CT-positive regions is an artifact due to the partial volume effect[39]. The goal of this study is to determine the specificity with which the ^{18}F-fluoride signal associates with microcalcifications and, furthermore, whether the PET signal is amplified due to increased surface area.

Since microcalcification detection lies below the resolution of current imaging modalities, and therefore is difficult to monitor *in vivo*, we previously developed a 3D collagen hydrogel platform, which allows the growth of microcalcifications to be followed *in vitro*[8]. In order to determine if the increased PET signal is due to signal amplification resulting from microcalcifications, and address the lingering controversy in the field, this study utilized a controllable 3D hydrogel model of fibrous cap to simulate microcalcification growth, as well as comparative *ex vivo* analysis of calcified human atherosclerotic plaques and a mouse model of atherosclerosis.

METHODS

The data and study materials will be available to other researchers for purposes of reproducing the results or replicating the procedure.

The following experiments were conducted in accordance with Brigham and Women's Hospital research policies. The Institutional Animal Care and Use committees at Beth Israel Deaconess Medical Center and at Brigham and Women's Hospital approved all animal procedures.

Calcium affinity study

To determine the affinity of calcium salts with markers of microcalcification, biologically relevant calcium salts found in atherosclerotic plaques were incubated with a near infrared fluorescence (NIRF) molecular imaging agent and the signals were quantified. Ten mg each of hydroxyapatite (Sigma-Aldrich, 289396-25G), calcium phosphate (Sigma-Aldrich, 900205-50G), calcium pyrophosphate (Sigma-Aldrich, 401552-25G), calcium oxalate (Sigma-Aldrich, 455997-5G) and calcium carbonate (Sigma-Aldrich, C4830-100G) were incubated with a NIRF calcium tracer (OsteoSense680, Perkin Elmer, NEV10020EX). The minerals were incubated with 1 ml of a 200-fold dilution of the stock solution for one hour at room temperature without light, in a rotator. Subsequently, they were washed 3 times with a 40-fold excess of PBS by centrifugation at 10.000 g for 15 minutes, followed by removal of the supernatant and resuspension with PBS. Afterwards they were imaged by fluorescence microscopy on an Eclipse 80i microscope (Nikon, Melville, NY, USA). Bright field and fluorescence images were taken and analyzed by thresholding for visible mineral crystals. Both values from bright field and fluorescence image analyses were matched per image taken to determine the fluorescence signal per amount of mineral.

An additional 10 mg of each of the minerals were incubated for one hour with 1 ml of ^{18}F-fluoride solution with an activity of 10 µCi/ml at room temperature without light in a rotator and afterwards was washed 3 times with a 40-fold excess of PBS. The radioactivity of the minerals was measured with a gamma well counter (Wizard2 Gamma Counter, Perkin Elmer) and the minerals were exposed overnight to a storage phosphor imaging plate for autoradiography.

In vitro microcalcification model

Human coronary artery smooth muscle cells (SMCs, PromoCell) passages 3-5 were grown to confluence and cultured in control media (DMEM with 10% fetal bovine serum and 1% penicillin/streptomycin) and in procalcifying media consisting of control media with the addition of 10 nM dexamethasone, 100 μM L-ascorbic acid, and 10 mM β-glycerophosphate. Media were replaced every 3 days. The culture media were replaced at 7, 14, and 21 days with media containing the same components, except that 0.1% fetal bovine serum was used to reduce noise caused by EVs present in the serum. After 24 hours, the 0.1% fetal bovine serum-media were collected and centrifuged for 5 min at 1,000 g to remove contaminants such as apoptotic bodies and cell debris. The resulting supernatant was stored at -80 °C.

Collagen hydrogels for *in vitro* formation of microcalcifications were prepared by slowly increasing the pH of concentrated rat tail collagen stored in an acetic acid solution (BD Biosciences) to 7-8, thereby leading to formation of a collagen network[8]. The previously collected and concentrated EVs were then added to the hydrogels and incubated for 5 days. The hydrogels were incubated with a NIRF calcium tracer overnight and imaged by fluorescence and confocal microscopy. For PET tracer analysis, the hydrogels were incubated for one hour with a solution of ^{18}F-fluoride with an activity of 1 μCi/ml, washed three times with PBS, and placed in reaction tubes. The activity was measured using a gamma well counter (Wizard2 Gamma Counter, Perkin Elmer).

18F-fluoride μPET-CT of carotid endarterectomy and coronary arteries specimens

Carotid artery specimens (n=2) were obtained with ethical approval and informed consent from patients undergoing carotid endarterectomy (National Health Service West of Scotland Research Ethics Committee 12/WS/0227). Atherosclerotic sections of left main coronary arteries (n=2) were obtained with ethical approval and informed relative authorization from the next of kin from victims of sudden death at the time of autopsy (National Health Service South East Scotland Research Ethics Committee 14/SS/1090). Tissue was immediately fresh frozen at -80 degrees Celsius.

Thawed non-decalcified carotid artery and coronary artery specimens were incubated for 60 minutes in ^{18}F-fluoride 100kBq/mL solution (10.5MBq ^{18}F-NaF in 99.5mLs 0.9% NaCl). Specimens were twice washed in 10mLs 0.9% NaCl for 5 minutes to remove unbound 18F-fluoride. Specimens were scanned using high-resolution μPET (1:5 coincidence mode) and CT (semi-circular full trajectory, maximum field of view, 480 projections, 50 kVp, 300 ms and 1:4 binning) (Mediso nanoScan PET/CT, Mediso Medical Imaging Systems, Hungary). PET data were reconstructed using Mediso's iterative Tera-Tomo 3D reconstruction algorithm using 4 iterations, 6 subsets, full detector model, normal regularization, spike filter on, voxel size 0·6 mm and 400-600 keV energy window. μPET-CT images were analyzed on an OsiriX workstation (OsiriX version 7.5.1, 64-bit, OsiriX Imaging Software, Geneva, Switzerland). μPET and μCT were acquired sequentially in the same field of view with no distortion of the alignment, thus ensuring direct co-localization of PET and CT datasets. Routine quality control/quality assurance procedures are performed on the preclinical PET/CT system to ensure that co-registration is within an acceptable range set by the manufacturer.

Histological Analyses

Samples were embedded in optimal cutting temperature compound (O.C.T.) and stored at -20 °C until use. Tissues were sectioned in areas that were PET-positive and CT-negative and cut into 5 μm thick sections for further analyses. NIRF calcium tracer was used in a 1:200 dilution in PBS and applied to the sections overnight and stored at 4 °C. Additional stains were used to identify calcifications within the sections and to verify the results of the NIRF tracer. In addition, we used von Kossa Stain (American MasterTech, KTVKO) to detect calcification. The tissue sections were fixed with formalin, covered in 5% silver nitrate solution, and then placed under UV light for 1 hour. The slides were then rinsed with 5% sodium thiosulfate and stained with Nuclear Red Fast stain. Finally, we used the VECTOR Red Alkaline Phosphatase Substrate kit (SK-5100) to detect osteogenic activity and early microcalcifications. We mixed the reagents included in the kit with 5

mL of 100mM Tris-HCl (pH 8.5) buffer as described in the product protocol. We covered the sections with the solution for 1 hour, and then rinsed the slides in Tris-HCl (pH 8.5) buffer. The samples were then stained for nuclei using Harris hematoxylin.

^{18}F-fluoride autoradiography of histological sections

Tissue sections for autoradiography were washed in PBS and incubated for one hour in ^{18}F-fluoride solution with an activity of 1 µCi/ml. Subsequently, the sections were again washed with PBS, dried, and exposed to a charged phosphorous plate overnight. The plate was scanned afterwards, and autoradiograms were compared to NIRF images of the same sections obtained using a Nikon A1 confocal microscope (Nikon, USA). The image was divided into four quadrants, and the total signal per quadrant was determined for both autoradiography and NIRF using the mean intensity value per quadrant. Values of identical quadrants were matched, and correlation was determined using the Pearson method.

Arterial calcification mouse model

30-week-old LDLr$^{-/-}$ male mice (n=10) that had been fed an atherogenic high-fat, high-cholesterol (HF/HC) diet (21% fat and 1.25% cholesterol, Research Diets D12108C, New Brunswick, NJ), a model of vascular calcification, for 15 weeks were studied. Age-matched wild-type C57BL/6 mice (n=5, Jackson Laboratory, Bar Harbor, ME) were used as controls. The Institutional Animal Care and Use committees at Beth Israel Deaconess Medical Center and at Brigham and Women's Hospital approved all animal procedures.

Mice were injected with a NIRF imaging agent (OsteoSense680, Perkin Elmer) 24 hours before aorta extraction. After euthanasia, aortas were perfused with saline, extracted and imaged with a fluorescence reflectance imaging (FRI) Kodak imager to determine the fluorescence signal. The aortas were then incubated for one hour in a solution of ^{18}F-fluoride with an activity of 10 µCi/ml. After washing three times with PBS, activity was measured using the well counter. The aortas

were dipped in deionized-H_2O and mounted onto platforms before the PET/CT scanning took place. After overnight storage at 4°, aortas were embedded in O.C.T. compound for further histological analyses.

Statistical Analysis

Quantitative data are given as mean ± standard deviation. The number of independent experiments is indicated as n. Statistical packages within GraphPad Prism were used to determine data normality and variance estimation. Differences between control and compound fluorescence signals were evaluated using the Kruskal-Wallis test with Dunn's multiple comparison test. The two-way ANOVA analysis was used for determining statistical significance across labeling methods and collagen concentration. The Welch's correction for t-tests was used for non-matching sample sizes. A linear Pearson correlation method was used for correlative analyses for NIRF vs. ^{18}F-fluoride measurements. Considering the user-defined image quadrant as a random effect, we modeled the correlation between NIRF vs. ^{18}F-fluoride for all quadrants combined ('nlme' R package). For each quadrant separately, we also tested whether any given histological section was an influential outlier by performing a Jackknife resampling method (Supplemental Material)[40]. For a variance component analysis (VCA), we employed the 'VCA' R package. P-values of $p<0.05$ were considered significant.

RESULTS

NIRF calcium tracer and ^{18}F-fluoride show preferential affinity for hydroxyapatite

The NIRF calcium tracer exhibited high affinity for hydroxyapatite when compared with calcium phosphate, calcium oxalate, and calcium carbonate (Fig. 1A). The NIRF calcium tracer exhibited some affinity for pyrophosphate, but affinity was 85% less than that of the hydroxyapatite.

Compared to hydroxyapatite, NIRF signal was reduced by 98.2% for calcium phosphate and 98.5% for calcium oxalate and calcium carbonate. ^{18}F-fluoride showed high affinity for hydroxyapatite at 13.9x10^5 counts per minute (CPM) when compared with calcium phosphate (0.27x10^5 CPM), calcium oxalate (0.13x10^5 CPM), and calcium carbonate (0.006x10^5 CMP) (Fig. 1B). ^{18}F-fluoride also showed decreased affinity for pyrophosphate by 36% at 8.91x10^5 CPM. Qualitative observations using fluorescence microscopy and autoradiography images (Fig. 1C and 1D) support these quantification results, displaying the highest signal in the hydroxyapatite samples. The ^{18}F-fluoride autoradiogram also showed signal for the calcium pyrophosphate to a lesser degree than that of the hydroxyapatite. These findings suggest that both ^{18}F-fluoride and the NIRF calcium tracer exhibit preferential binding for hydroxyapatite.

In vitro microcalcification model

To assess the specificity of the ^{18}F-fluoride signal in an *in vitro* collagen hydrogel model of microcalcification formation, we used a mixture of radioactively labeled ^{18}F-fluoride and unlabeled fluoride (Cold NaF) to test for nonspecific binding of the tracer to microcalcifications. Hydrogels incubated with ^{18}F-fluoride (Hot NaF) exhibited significantly higher radioactive counts per minute (CPM) compared to untreated control hydrogels and hydrogels incubated with the Cold NaF mixture ($p=0.0014$). Our previous work demonstrated that microcalcifications grown *in vitro* decrease in size as collagen concentration increases[8]. Similar to that study, smaller and more numerous microcalcifications were observed with a NIRF calcium tracer in hydrogels with higher collagen content (Fig. 2B). Autoradiography images indicated increased ^{18}F-fluoride signal associated with the smaller microcalcifications in the collagen-rich hydrogels (Fig. 2C). This suggests that an increase in the surface area of microcalcifications, due to an increase in the number of smaller microcalcifications (0.5 mg/ml collagen hydrogel), compared to fewer, larger microcalcifications (0.25 mg/ml collagen hydrogel), correlates with an increase in ^{18}F-fluoride PET signal.

PET/CT of carotid endarterectomy and coronary artery specimens

Explanted carotid endarterectomy and coronary artery (Fig. 3A) samples (n=4) were incubated in 100kBq/mL ^{18}F-fluoride and imaged using μPET-CT. Fused μPET/CT images of *ex vivo* coronary artery showed high ^{18}F-fluoride activity in areas of coronary artery without CT-macrocalcification (Fig. 3B, 3C, 3D) with axial reconstruction confirming that binding colocalizes to discrete regions in the coronary artery wall (Fig. 3E). 3D volume rendered casts of *ex vivo* carotid endarterectomy specimens demonstrated ^{18}F-fluoride binding to the samples with (Fig. 3F, G, I) and without macrocalcification (Fig. 3J, K and L). Transverse view of PET/CT images confirmed ^{18}F-fluoride binding to the surface of exposed macrocalcified regions and non-calcified regions of the artery wall (Fig. 3H, I, and K (inset), and L (inset)). The discrete signal of ^{18}F-fluoride activity in non-calcified regions (PET-positive/CT-negative) suggests that ^{18}F-fluoride binding cannot be explained by the presence of macrocalcification alone.

Histological analyses of PET-positive and CT-negative areas of carotid endarterectomy samples

Staining of PET-positive and CT-negative regions of carotid endarterectomy samples with a NIRF calcium tracer revealed the presence of microcalcifications within the sections (Fig. 4A). Autoradiography of consecutive sections after incubation with ^{18}F-fluoride showed similar patterns of intensity-rich areas (Fig. 4B and 4C). The sections were visually aligned and the images were divided into quadrants to compare the fluorescent and PET signal intensities (Fig. 4D). A correlation analysis revealed a strong correlation between the fluorescence of the NIRF calcium tracer and ^{18}F-fluoride (Fig. 4E; Pearson R = 0.8048, p = 0.0124).

MicroPET/CT scan of calcified murine aortas

NIRF molecular imaging of extracted murine aortas exhibited larger calcification areas within the LDLr$^{-/-}$ mouse aortas (0.28; n=7) compared to the aortas of wildtype mice (0.05; n=3) (WT, C57BL/6 mice, p<0.0001; Fig. 5A). The LDLr$^{-/-}$ mouse aortas also exhibited higher positron

emission signals ($1.03x10^5$ CPM; n=7) than WT mouse aortas ($0.08x10^5$ CPM; n=3) after incubation with ^{18}F-fluoride ($p<0.0001$; Fig. 5B). μPET/CT scans of the aortas showed regions of high PET signal that were comparable to signal-rich areas within the fluorescence images (Fig. 5C). To validate the detection of calcified areas with μPET/CT, histological analyses were performed on the aorta sections with high PET signal and fluorescence. The results confirmed the presence of macro-scale and micro-scale calcifications within the aorta, which correlate with fluorescence and PET imaging (Fig. 5C).

Discussion

The salient new findings from this study are that regions identified as PET-positive and CT-negative with ^{18}F-fluoride PET/CT imaging are due to the presence of developing microcalcifications within atherosclerotic plaque. ^{18}F-fluoride and the NIRF molecular imaging showed preferentially high affinity for hydroxyapatite when compared with other biologically relevant calcium salts. The NIRF calcium tracer is already a well-established marker for cardiovascular calcification. Specifically, it has been demonstrated to visualize early microcalcifications in human samples and preclinical mouse models [8, 31, 41, 42]. Therefore, we used this NIRF tracer as a corroborative marker for comparison to ^{18}F-fluoride in *ex vivo* and *in vitro* settings. ^{18}F-Fluoride is a highly sensitive radiotracer that has been used in oncological practice to image bone tumors[4, 9, 43]. More recently it has been found to exhibit uptake in atherosclerotic aorta and coronary arteries[44, 45]. Hydroxyapatite is a primary constituent of vascular calcification[31], and the ^{18}F-fluoride ion is incorporated into the hydroxyapatite structure through an exchange of the hydroxyl groups on the surface of the mineral resulting in fluorapatite[35, 46, 47].

^{18}F-fluoride has favorable imaging properties as well, including minimal dissociation, tissue contrast between labeled and un-labeled tissues one hour after administration, rapid binding, and low radiotracer background[21]. The calcific portions of atherosclerotic plaque absorb ^{18}F-fluoride

selectively, with high affinity both *in vitro* and *in vivo*, and with no fluoride activity detected in the absence of calcification[1, 15, 32]. The ^{18}F-fluoride ligand binds to the surface of the calcification, and the increased surface area of microcalcifications allows for better absorption[15]. In contrast, there is proportionally smaller radioactivity signal detected for macrocalcifications[1, 15, 45, 46].

In this study, ^{18}F-fluoride demonstrated an affinity for cell-derived hydroxyapatite associated microcalcifications developed *in vitro* in a 3D collagen hydrogel system. When combined with unlabeled fluoride, ^{18}F-fluoride demonstrated specific binding for microcalcifications in the hydrogels. Additionally, the presence of these calcifications was confirmed with a NIRF calcium tracer, a current imaging standard in calcification cardiovascular research. These results suggest that the ^{18}F-fluoride tracer has the same affinity for organic hydroxyapatite derived from calcifying EVs from vascular smooth muscle cells. Our previous studies have demonstrated that hydrogels with a greater concentration of collagen have denser collagen networks and therefore limit the size to which microcalcifications can aggregate[8]. This results in an increase in the surface area of hydroxyapatite, if the total amount of calcification remains the same. Smaller, more numerous microcalcifications form as the collagen concentration increases. It was found that higher concentrations of collagen displayed higher levels of ^{18}F-fluoride, suggesting that an amplification in ^{18}F-fluoride signal is seen with the increased surface area.

In *ex vivo* carotid endarterectomy samples and coronary artery samples, a ^{18}F-fluoride PET signal is seen not just in areas of calcification, as identified by simultaneous CT imaging, but in non-calcified areas, both adjacent to and distal from calcifications. These results are consistent with those reported in earlier studies[9, 21, 35, 48]. The histological analyses of the areas with positive PET signal and negative CT signal revealed the presence of microcalcifications. This was first confirmed with the use of molecular imaging with NIRF calcium tracer, which is able to fluorescently tag microcalcifications. Adjacent tissue sections incubated with ^{18}F-fluoride displayed a similar pattern of signal, and a significant correlation was observed between both ^{18}F-

fluoride and the NIRF signal. These findings suggest that the amplified PET signal that was observed in non-calcified areas of *ex vivo* sections was due to the presence of microcalcifications that were not detected by CT imaging. The amplification of the signal is likely due to the increased surface area of the microcalcifications.

Comparison of *in vivo* ^{18}F-fluoride μPET/CT imaging with *ex vivo* NIRF molecular imaging of atherosclerotic mouse aortas, demonstrated a similar signal pattern with correlation observed between the techniques. Histological analysis of the tissue sections with positive ^{18}F-fluoride signal confirmed the presence of calcification. Alkaline phosphatase staining for early osteogenic activity and staining with NIRF calcium tracer both displayed relatively more signal when compared with von Kossa staining that detects phosphate groups in mature hydroxyapatite crystals. However, alkaline phosphatase and NIRF calcium stains are known to be more sensitive than von Kossa staining[31] and might indicate early-stage microcalcification. These findings suggest that ^{18}F-fluoride μPET/CT can identify microcalcifications *in vivo* and that the microcalcifications are the reason for PET signal amplification.

Notably, ^{18}F-fluoride uptake has been associated with patient populations with greater cardiovascular risk factor burden. ^{18}F-fluoride PET/CT detects microcalcification in patients with unstable manifestations of coronary atherosclerosis[6, 10, 15, 32, 35], and patients with ^{18}F-fluoride uptake are more likely to have an increase in Framingham risk prediction scores, previous major adverse cardiac events, established coronary artery disease, angina, and revascularization[9]. The relatively low cost of the ligand and the excellent interobserver repeatability make it a strong candidate for clinical use[35]. Although it has been postulated that PET positive regions extending beyond CT positive regions can represent an artifact caused by partial-volume effects[39], our study demonstrates that the ^{18}F-fluoride signal is associated with microcalcifications too small to be detected by CT-imaging. The data show that the ^{18}F-fluoride ligand tags microcalcifications in a controllable 3D hydrogel model of fibrous cap progressively with increased surface area of

microcalcifications, and that these results can be translated to *ex vivo* analysis of human tissues, as well as mouse models of atherosclerosis. Our *ex vivo* incubation model may not exactly recreate *in vivo* conditions where 18F-fluoride is delivered intravenously and where partial volume effects may affect the coronary signal. Further work needs to be done to differentiate between false positives and false negatives in ^{18}F-fluoride PET/CT imaging; however, it is highly likely that ^{18}F-fluoride signal in PET-positive and CT-negative regions is due to the presence of microcalcifications. Additionally, further studies are required to determine if these results are possibly due to an increase in the surface area of the overall calcification.

^{18}F-fluoride PET/CT might have a role in evaluating patients with atherosclerotic disease, particularly by identifying areas of microcalcification in coronary arteries, implying the presence of vulnerable or recently ruptured plaques. Two ongoing clinical trials are using this radiotracer to assess whether ^{18}F-fluoride has prognostic utility in patients with myocardial infarction (NCT02278211) and if ^{18}F-fluoride can be used to stratify patients to emerging therapeutic interventions (NCT02110303). This manuscript adds to the growing body of knowledge that plaque mineralization is an active process and may be a target for clinical intervention. Early detection of unstable plaques could facilitate initiation and modulation of treatment to help prevent cardiovascular events. In conclusion, the findings of this study suggest that areas of microcalcification in developing atherosclerotic plaques are highly correlated with signal amplification of the ^{18}F-fluoride ligand when imaged with ^{18}F-fluoride PET/CT.

Acknowledgements: The authors thank Jennifer Wen for her skillful histological assistance.

Funding: Dr. Elena Aikawa is supported by National Institutes of Health (NIH) grants R01HL 114805 and R01HL 136431. Dr. Joshua Hutcheson is supported by a Scientist Development

Grant from the American Heart Association (17SDG633670259). Dr. Alastair J. Moss and Dr. David E. Newby are supported by a Wellcome Trust Senior Investigator Award (WT103782/Z/14/Z) and a Chief Scientific Office grant (CGA/17/53). Dr. Marc R. Dweck is supported by the British Heart Foundation (FS/14/78/31020) and the Sir Jules Thorn Charitable Trust [15/JTA]. Adriana A.S. Tavares is supported by the British Heart Foundation (RG/16/10/32375). Dr. Marcelo Di Carli is supported by NIH grant R01HL 132021.

Disclosures: None.

REFERENCES

1. Greenland P, LaBree L, Azen SP, Doherty TM and Detrano RC. Coronary artery calcium score combined with Framingham score for risk prediction in asymptomatic individuals. *Jama*. 2004;291:210-5.
2. Detrano R, Guerci AD, Carr JJ, Bild DE, Burke G, Folsom AR, Liu K, Shea S, Szklo M, Bluemke DA, O'Leary DH, Tracy R, Watson K, Wong ND and Kronmal RA. Coronary calcium as a predictor of coronary events in four racial or ethnic groups. *The New England journal of medicine*. 2008;358:1336-45.
3. Hecht HS, Cronin P, Blaha MJ, Budoff MJ, Kazerooni EA, Narula J, Yankelevitz D and Abbara S. 2016 SCCT/STR guidelines for coronary artery calcium scoring of noncontrast noncardiac chest CT scans: A report of the Society of Cardiovascular Computed Tomography and Society of Thoracic Radiology. *Journal of cardiovascular computed tomography*. 2017;11:74-84.
4. Adamson PD, Vesey AT, Joshi NV, Newby DE and Dweck MR. Salt in the wound: (18)F-fluoride positron emission tomography for identification of vulnerable coronary plaques. *Cardiovasc Diagn Ther*. 2015;5:150-5.
5. O'Brien KD, Kuusisto J, Reichenbach DD, Ferguson M, Giachelli C, Alpers CE and Otto CM. Osteopontin is expressed in human aortic valvular lesions. *Circulation*. 1995;92:2163-8.
6. Chen W and Dilsizian V. Targeted PET/CT imaging of vulnerable atherosclerotic plaques: microcalcification with sodium fluoride and inflammation with fluorodeoxyglucose. *Curr Cardiol Rep*. 2013;15:364.
7. New SE, Goettsch C, Aikawa M, Marchini JF, Shibasaki M, Yabusaki K, Libby P, Shanahan CM, Croce K and Aikawa E. Macrophage-derived matrix vesicles: an alternative novel mechanism for microcalcification in atherosclerotic plaques. *Circ Res*. 2013;113:72-7.
8. Hutcheson JD, Goettsch C, Bertazzo S, Maldonado N, Ruiz JL, Goh W, Yabusaki K, Faits T, Bouten C, Franck G, Quillard T, Libby P, Aikawa M, Weinbaum S and Aikawa E. Genesis and growth of extracellular-vesicle-derived microcalcification in atherosclerotic plaques. *Nat Mater*. 2016;15:335-43.
9. Dweck MR, Chow MW, Joshi NV, Williams MC, Jones C, Fletcher AM, Richardson H, White A, McKillop G, van Beek EJ, Boon NA, Rudd JH and Newby DE. Coronary arterial 18F-sodium fluoride uptake: a novel marker of plaque biology. *J Am Coll Cardiol*. 2012;59:1539-48.
10. Huang H, Virmani R, Younis H, Burke AP, Kamm RD and Lee RT. The impact of calcification on the biomechanical stability of atherosclerotic plaques. *Circulation*. 2001;103:1051-6.
11. Ehara S, Kobayashi Y, Yoshiyama M, Shimada K, Shimada Y, Fukuda D, Nakamura Y, Yamashita H, Yamagishi H, Takeuchi K, Naruko T, Haze K, Becker AE, Yoshikawa J and Ueda M. Spotty calcification typifies the culprit plaque in patients with acute myocardial infarction: an intravascular ultrasound study. *Circulation*. 2004;110:3424-9.
12. Vengrenyuk Y, Carlier S, Xanthos S, Cardoso L, Ganatos P, Virmani R, Einav S, Gilchrist L and Weinbaum S. A hypothesis for vulnerable plaque rupture due to stress-induced debonding around cellular microcalcifications in thin fibrous caps. *Proc Natl Acad Sci U S A*. 2006;103:14678-83.
13. McEvoy JW, Blaha MJ, Defilippis AP, Budoff MJ, Nasir K, Blumenthal RS and Jones SR. Coronary artery calcium progression: an important clinical measurement? A review of published reports. *J Am Coll Cardiol*. 2010;56:1613-22.
14. Stary HC, Chandler AB, Dinsmore RE, Fuster V, Glagov S, Insull W, Jr., Rosenfeld ME, Schwartz CJ, Wagner WD and Wissler RW. A definition of advanced types of atherosclerotic lesions and a histological classification of atherosclerosis. A report from the Committee on Vascular Lesions of the Council on Arteriosclerosis, American Heart Association. *Arterioscler Thromb Vasc Biol*. 1995;15:1512-31.
15. Ueda M. [Clinical relevance of coronary artery calcification, as a risk factor for plaque rupture: viewpoint from pathology]. *Clin Calcium*. 2010;20:1656-62.

16. Kelly-Arnold A, Maldonado N, Laudier D, Aikawa E, Cardoso L and Weinbaum S. Revised microcalcification hypothesis for fibrous cap rupture in human coronary arteries. *Proc Natl Acad Sci U S A*. 2013;110:10741-6.
17. Budoff MJ and Gul KM. Expert review on coronary calcium. *Vasc Health Risk Manag*. 2008;4:315-24.
18. Bastos Goncalves F, Voute MT, Hoeks SE, Chonchol MB, Boersma EE, Stolker RJ and Verhagen HJ. Calcification of the abdominal aorta as an independent predictor of cardiovascular events: a meta-analysis. *Heart*. 2012;98:988-94.
19. Schmid K, McSharry WO, Pameijer CH and Binette JP. Chemical and physicochemical studies on the mineral deposits of the human atherosclerotic aorta. *Atherosclerosis*. 1980;37:199-210.
20. Raggi P, Callister TQ and Shaw LJ. Progression of coronary artery calcium and risk of first myocardial infarction in patients receiving cholesterol-lowering therapy. *Arterioscler Thromb Vasc Biol*. 2004;24:1272-7.
21. Irkle A, Vesey AT, Lewis DY, Skepper JN, Bird JL, Dweck MR, Joshi FR, Gallagher FA, Warburton EA, Bennett MR, Brindle KM, Newby DE, Rudd JH and Davenport AP. Identifying active vascular microcalcification by (18)F-sodium fluoride positron emission tomography. *Nat Commun*. 2015;6:7495.
22. Murray CJ and Lopez AD. Measuring the global burden of disease. *The New England journal of medicine*. 2013;369:448-57.
23. Vliegenthart R, Oudkerk M, Hofman A, Oei HH, van Dijck W, van Rooij FJ and Witteman JC. Coronary calcification improves cardiovascular risk prediction in the elderly. *Circulation*. 2005;112:572-7.
24. Martin SS, Blaha MJ, Blankstein R, Agatston A, Rivera JJ, Virani SS, Ouyang P, Jones SR, Blumenthal RS, Budoff MJ and Nasir K. Dyslipidemia, coronary artery calcium, and incident atherosclerotic cardiovascular disease: implications for statin therapy from the multi-ethnic study of atherosclerosis. *Circulation*. 2014;129:77-86.
25. Doherty TM, Asotra K, Fitzpatrick LA, Qiao JH, Wilkin DJ, Detrano RC, Dunstan CR, Shah PK and Rajavashisth TB. Calcification in atherosclerosis: bone biology and chronic inflammation at the arterial crossroads. *Proc Natl Acad Sci U S A*. 2003;100:11201-6.
26. Cocker MS, Spence JD, Hammond R, Wells G, deKemp RA, Lum C, Adeeko A, Yaffe MJ, Leung E, Hill A, Nagpal S, Stotts G, Alturkustani M, Hammond L, DaSilva J, Hadizad T, Tardif JC, Beanlands RS and Canadian Atherosclerosis Imaging N. [(18)F]-NaF PET/CT Identifies Active Calcification in Carotid Plaque. *JACC Cardiovasc Imaging*. 2017;10:486-488.
27. Budoff MJ, Shaw LJ, Liu ST, Weinstein SR, Mosler TP, Tseng PH, Flores FR, Callister TQ, Raggi P and Berman DS. Long-term prognosis associated with coronary calcification: observations from a registry of 25,253 patients. *J Am Coll Cardiol*. 2007;49:1860-70.
28. London GM, Guerin AP, Marchais SJ, Metivier F, Pannier B and Adda H. Arterial media calcification in end-stage renal disease: impact on all-cause and cardiovascular mortality. *Nephrol Dial Transplant*. 2003;18:1731-40.
29. Stary HC. Natural history of calcium deposits in atherosclerosis progression and regression. *Z Kardiol*. 2000;89 Suppl 2:28-35.
30. Ritman EL. Small-animal CT - Its Difference from, and Impact on, Clinical CT. *Nucl Instrum Methods Phys Res A*. 2007;580:968-970.
31. Aikawa E, Nahrendorf M, Figueiredo JL, Swirski FK, Shtatland T, Kohler RH, Jaffer FA, Aikawa M and Weissleder R. Osteogenesis associates with inflammation in early-stage atherosclerosis evaluated by molecular imaging in vivo. *Circulation*. 2007;116:2841-50.
32. Attizzani GF, Patricio L and Bezerra HG. Optical coherence tomography assessment of calcified plaque modification after rotational atherectomy. *Catheterization and cardiovascular interventions : official journal of the Society for Cardiac Angiography & Interventions*. 2013;81:558-61.

33. Virmani R, Burke AP, Farb A and Kolodgie FD. Pathology of the vulnerable plaque. *J Am Coll Cardiol*. 2006;47:C13-8.
34. Libby P, DiCarli M and Weissleder R. The vascular biology of atherosclerosis and imaging targets. *J Nucl Med*. 2010;51 Suppl 1:33S-37S.
35. Joshi NV, Vesey AT, Williams MC, Shah AS, Calvert PA, Craighead FH, Yeoh SE, Wallace W, Salter D, Fletcher AM, van Beek EJ, Flapan AD, Uren NG, Behan MW, Cruden NL, Mills NL, Fox KA, Rudd JH, Dweck MR and Newby DE. 18F-fluoride positron emission tomography for identification of ruptured and high-risk coronary atherosclerotic plaques: a prospective clinical trial. *Lancet*. 2014;383:705-13.
36. Even-Sapir E, Metser U, Mishani E, Lievshitz G, Lerman H and Leibovitch I. The detection of bone metastases in patients with high-risk prostate cancer: 99mTc-MDP Planar bone scintigraphy, single- and multi-field-of-view SPECT, 18F-fluoride PET, and 18F-fluoride PET/CT. *J Nucl Med*. 2006;47:287-97.
37. Blau M, Nagler W and Bender MA. Fluorine-18: a new isotope for bone scanning. *J Nucl Med*. 1962;3:332-4.
38. Watson KE, Bostrom K, Ravindranath R, Lam T, Norton B and Demer LL. TGF-beta 1 and 25-hydroxycholesterol stimulate osteoblast-like vascular cells to calcify. *J Clin Invest*. 1994;93:2106-13.
39. Demer LL, Tintut Y, Nguyen KL, Hsiai T and Lee JT. Rigor and Reproducibility in Analysis of Vascular Calcification. *Circ Res*. 2017;120:1240-1242.
40. Efron B and Tibshirani RJ. *An introduction to the bootstrap*: CRC press; 1994.
41. Aikawa E, Aikawa M, Libby P, Figueiredo JL, Rusanescu G, Iwamoto Y, Fukuda D, Kohler RH, Shi GP, Jaffer FA and Weissleder R. Arterial and aortic valve calcification abolished by elastolytic cathepsin S deficiency in chronic renal disease. *Circulation*. 2009;119:1785-94.
42. Hjortnaes J, Butcher J, Figueiredo JL, Riccio M, Kohler RH, Kozloff KM, Weissleder R and Aikawa E. Arterial and aortic valve calcification inversely correlates with osteoporotic bone remodelling: a role for inflammation. *Eur Heart J*. 2010;31:1975-84.
43. Grant FD, Fahey FH, Packard AB, Davis RT, Alavi A and Treves ST. Skeletal PET with 18F-fluoride: applying new technology to an old tracer. *J Nucl Med*. 2008;49:68-78.
44. Derlin T, Richter U, Bannas P, Begemann P, Buchert R, Mester J and Klutmann S. Feasibility of 18F-sodium fluoride PET/CT for imaging of atherosclerotic plaque. *J Nucl Med*. 2010;51:862-5.
45. Beheshti M, Saboury B, Mehta NN, Torigian DA, Werner T, Mohler E, Wilensky R, Newberg AB, Basu S, Langsteger W and Alavi A. Detection and global quantification of cardiovascular molecular calcification by fluoro18-fluoride positron emission tomography/computed tomography--a novel concept. *Hell J Nucl Med*. 2011;14:114-20.
46. Blau M, Ganatra R and Bender MA. 18 F-fluoride for bone imaging. *Semin Nucl Med*. 1972;2:31-7.
47. Hawkins RA, Choi Y, Huang SC, Hoh CK, Dahlbom M, Schiepers C, Satyamurthy N, Barrio JR and Phelps ME. Evaluation of the skeletal kinetics of fluorine-18-fluoride ion with PET. *J Nucl Med*. 1992;33:633-42.
48. Dweck MR, Khaw HJ, Sng GK, Luo EL, Baird A, Williams MC, Makiello P, Mirsadraee S, Joshi NV, van Beek EJ, Boon NA, Rudd JH and Newby DE. Aortic stenosis, atherosclerosis, and skeletal bone: is there a common link with calcification and inflammation? *Eur Heart J*. 2013;34:1567-74.

Figure Legends

Figure 1. Affinity study of calcium salts with two markers for microcalcification - a near infrared fluorescence (NIRF) calcium tracer, and ^{18}F-fluoride. **A,** Signal quantification of NIRF tracer for individual calcium salts, and a Kruskal-Wallis test with Dunn's multiple comparison test: Control – no mineral added (0.0±0.0, 0.0% of HA), HA – Hydroxyapatite (0.422±0.304, $p<0.0001$), PO_4 – Calcium Phosphate (0.008±0.011, 1.8% of HA, $p=0.1625$), PP – Calcium Pyrophosphate (0.062±0.066, 14.8% of HA, $p<0.001$), Ox – Calcium Oxalate (0.006±0.008, 1.5% of HA, $p=0.0133$), CO_3 – Calcium Carbonate (0.006±0.008, 1.5% of HA, $p=0.1237$). **B,** Signal quantification of radioactively labelled ^{18}F-fluoride for different calcium salts, and a Kruskal-Wallis test with Dunn's multiple comparison test: Control ($0.007x10^5$±$0.010x10^5$ CPM, 0.05% of HA), HA ($13.9x10^5$±$0.7x10^5$ CPM, $p=0.0066$), PO_4 ($0.27x10^5$±$0.08x10^5$ CPM, 1.9% of HA, $p=0.3323$), PP ($8.91x10^5$±$0.94x10^5$ CPM, 64.0% of HA, $p=0.0581$), Ox ($0.13x10^5$±$0.01x10^5$ CPM, 0.9% of HA, $p>0.9999$), CO_3 ($0.006x10^5$±$0.005x10^5$ CPM, 0.04% of HA, $p>0.9999$). **C,** Fluorescence images of different calcium salts after incubation with NIRF calcium tracer (scale bars, 100 μm). **D,** Autoradiograms of different calcium salts after incubation with ^{18}F-fluoride (scale bars, 0.25 mm).

Figure 2. Collagen hydrogels demonstrate affinity of ^{18}F-fluoride for microcalcifications. **A,** Quantification of radioactive signal of ^{18}F-NaF bound to microcalcifications within collagen hydrogels of two different collagen concentrations and two-way ANOVA analysis. Control – collagen hydrogels incubated without extracellular vesicles (0.25 mg/ml - $0.88x10^2$±$0.02x10^2$ CPM; 0.5 mg/ml - $0.85x10^2$±$0.04\ x10^2$ CPM). Cold NaF - a mixture of radioactively labeled ^{18}F-fluoride and unlabeled fluoride to test for nonspecific binding of the tracer to microcalcifications (0.25 mg/ml - $2.59x10^2$±$1.62x10^2$ CPM; 0.5 mg/ml - $5.67x10^2$±$2.79x10^2$ CPM). Hot NaF – radioactively labeled ^{18}F-fluoride for total binding (0.25 mg/ml - $33.8x10^2$±$12.4x10^2$ CPM; 0.5 mg/ml - $67.7x10^2$±$37.4x10^2$ CPM) ($p=0.0014$). P-value of the labeling method = 0.0014, p-value associated with collagen concentration = 0.2119, p-value of the interaction = 0.2956. **B,**

Fluorescence microscopy of microcalcifications in collagen hydrogels with microcalcifications after incubation with bisphosphonate-based fluorescent tracer (scale bars 100 μm). Two different collagen concentrations were used for the hydrogels. **C,** NIRF and autoradiography of microcalcifications in 3D collagen hydrogels after incubation with a NIRF tracer or ^{18}F-fluoride, respectively (scale bars 10 mm).

Figure 3. Coronary artery (a-e) and carotid endarterectomy specimens (f-l) 18F-fluoride μPET/CT. A, Explanted coronary artery specimens were incubated in 100kBq/mL 18F-fluoride (t=60 mins). **B,** 3-dimensional volume rendered casts colocalizes binding to coronary artery sections with paucity of uptake in the surrounding epicardial fat and myocardium **C,** μCT and, **D,** fused images enabled, **E,** detailed axial reconstruction of ^{18}F-fluoride binding in non-calcified coronary artery walls. **F & J,** 3-dimensional volume rendered casts of ^{18}F-fluoride binding in explanted carotid artery specimens. **G & K,** sagittal CT colocalizes ^{18}F-fluoride binding to exposed surfaces of hydroxyapatite on macrocalcified tissue. **H, I, K (inset) & I (inset),** focal ^{18}F-fluoride binding is present in non-calcified regions of the carotid artery wall.

Figure 4. Quantitative histological analysis of PET-positive/CT-negative areas of carotid endarterectomy sample A, Location of section taken for histological analysis of carotid endarterectomy sample. **B,** Confocal microscopy imaging of carotid endarterectomy section after incubation with a NIRF calcium tracer (scale bar 2 mm). **C,** Autoradiography imaging of the same histological section after incubation with ^{18}F-fluoride (scale bar 2 mm). **D,** Confocal and autoradiography images were divided into four quadrants and each quadrant of the images was quantified (scale bars 2 mm). **E,** Linear correlation between NIRF signal and ^{18}F-fluoride autoradiography signal (Pearson R = 0.8048, p = 0.0124; n = 6 histological sections were analyzed).

Figure 5. μPET/CT scan of calcified murine aortas shows presence of macro- and microcalcification and correlation between NIRF and PET signals. A, *Ex vivo* fluorescence, and **B,** *ex vivo* autoradiography imaging quantification of the calcified fraction of murine aortas for knockout ($p<0.0001$, Welch's t-test of log2(CPM) values) **C,** Respective murine aortic regions were sectioned and stained with von Kossa, ALP, and NIRF tracers to confirm the presence of calcification. Stains show consecutive sections (5 μm) (scale bars, NIRF and μPET/CT = 5 mm; von Kossa, ALP, and NIRF = 200 μm).

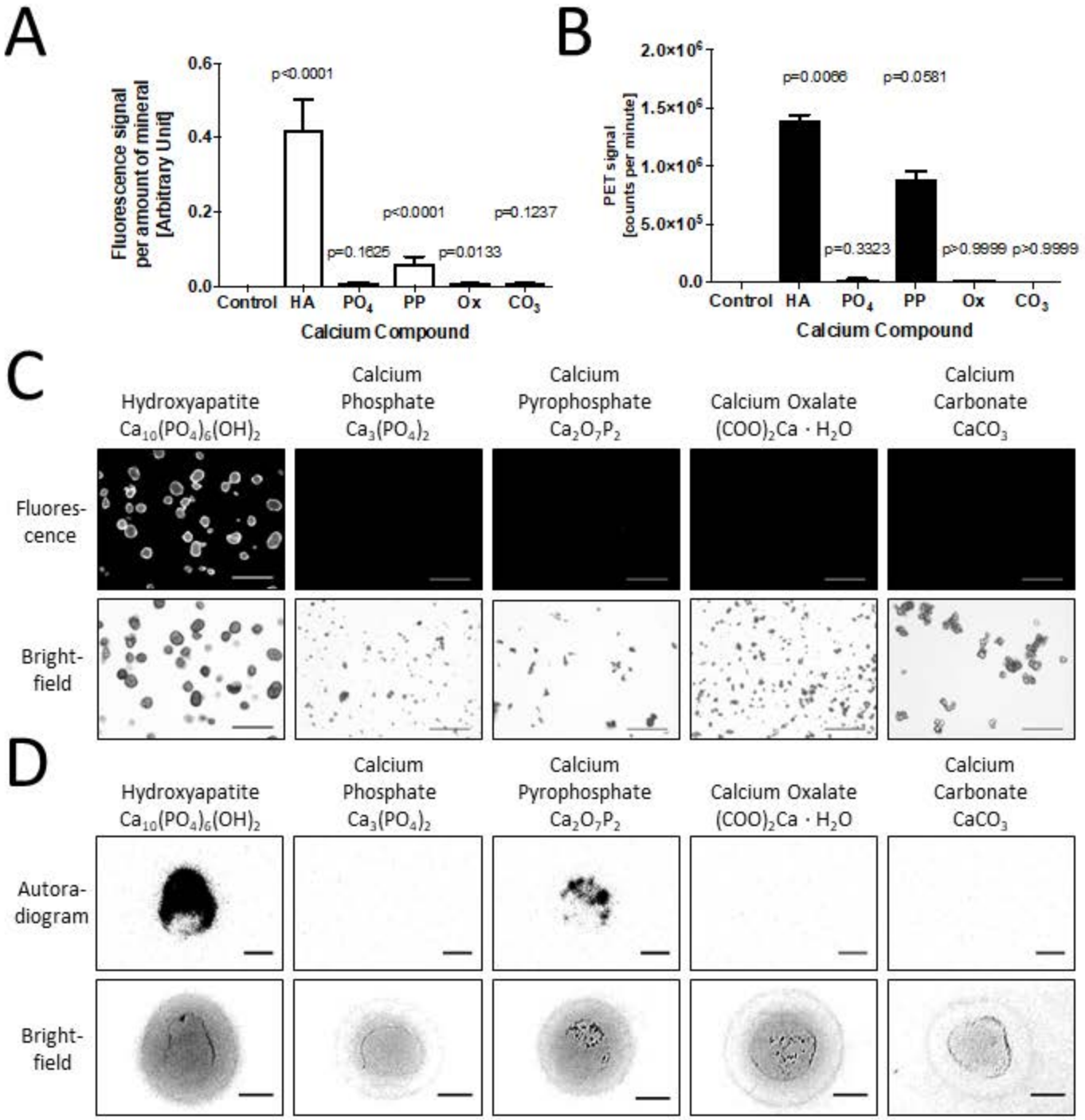
A
Fluorescence signal per amount of mineral [Arbitrary Unit]
0.6
0.4
0.2
0.0
p<0.0001
p=0.1625
p<0.0001
p=0.0133
p=0.1237
Control
HA
PO4
PP
Ox
CO3
Calcium Compound
B
PET signal [counts per minute]
2.0×10^6
1.5×10^6
1.0×10^6
5.0×10^5
0.0
p=0.0066
p=0.0581
p=0.3323
p>0.9999
p>0.9999
Control
HA
PO4
PP
Ox
CO3
Calcium Compound
C
Hydroxyapatite Ca10(PO4)6(OH)2
Calcium Phosphate Ca3(PO4)2
Calcium Pyrophosphate Ca2O7P2
Calcium Oxalate (COO)2Ca · H2O
Calcium Carbonate CaCO3
Fluores-cence
Bright-field
D
Hydroxyapatite Ca10(PO4)6(OH)2
Calcium Phosphate Ca3(PO4)2
Calcium Pyrophosphate Ca2O7P2
Calcium Oxalate (COO)2Ca · H2O
Calcium Carbonate CaCO3
Autora-diogram
Bright-field

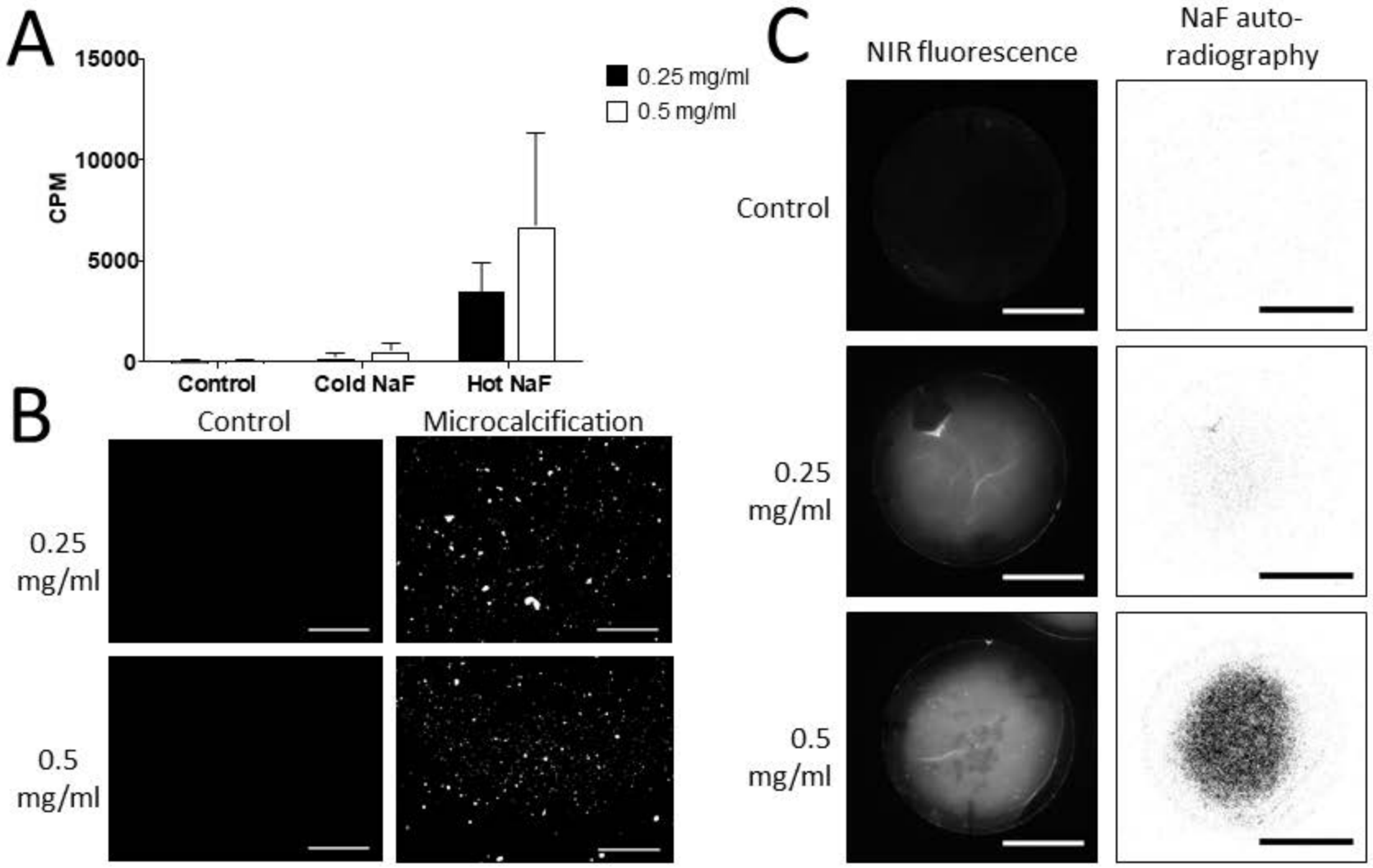
A
15000
10000
5000
0
CPM
0.25 mg/ml
0.5 mg/ml
Control
Cold NaF
Hot NaF
B
Control
Microcalcification
0.25 mg/ml
0.5 mg/ml
C
NIR fluorescence
NaF auto-radiography
Control
0.25 mg/ml
0.5 mg/ml

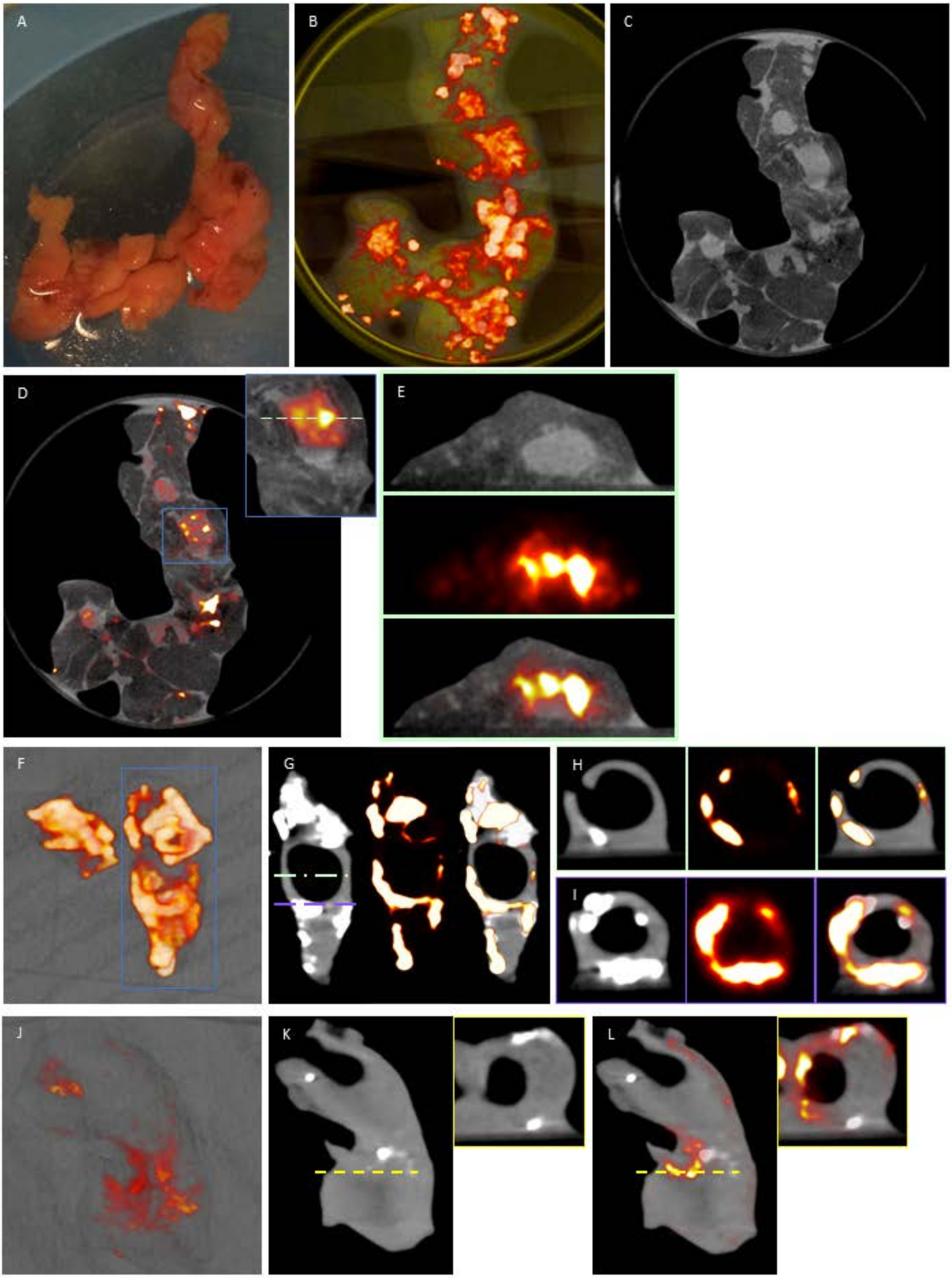
A
B
C
D
E
F
G
H
I
J
K
L

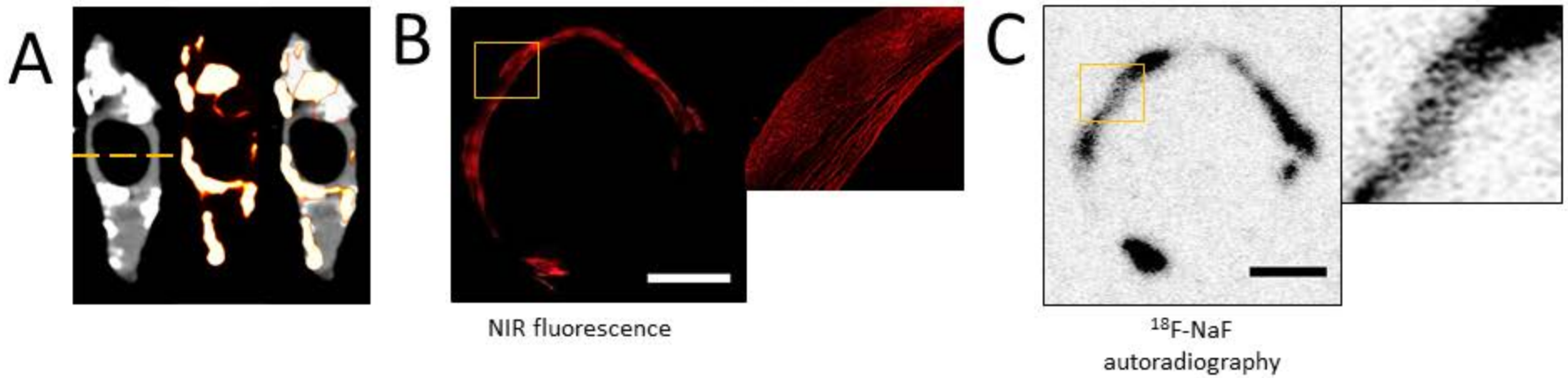
A
B
C
NIR fluorescence
18F-NaF
autoradiography

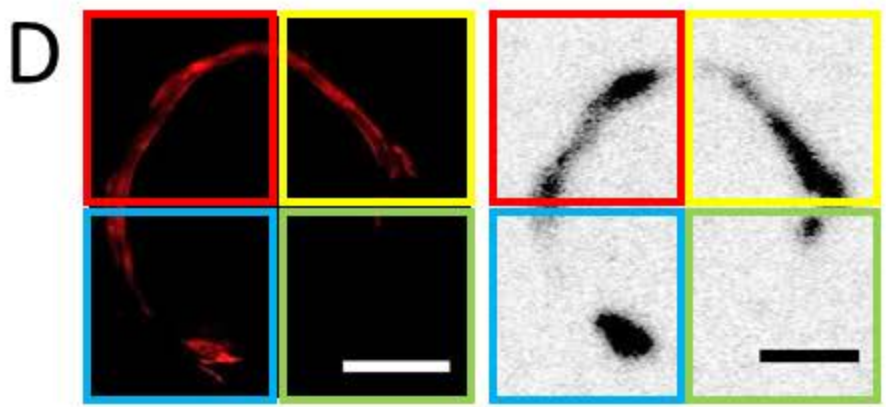
D

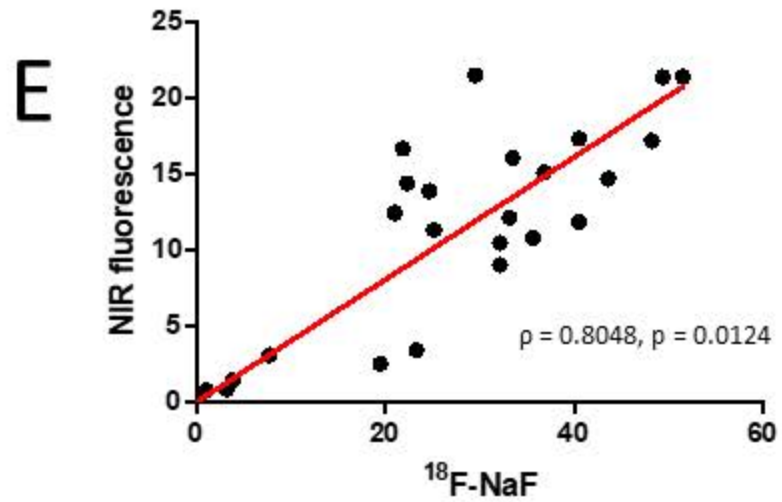
E
NIR fluorescence
18F-NaF
ρ = 0.8048, p = 0.0124
0
5
10
15
20
25
0
20
40
60

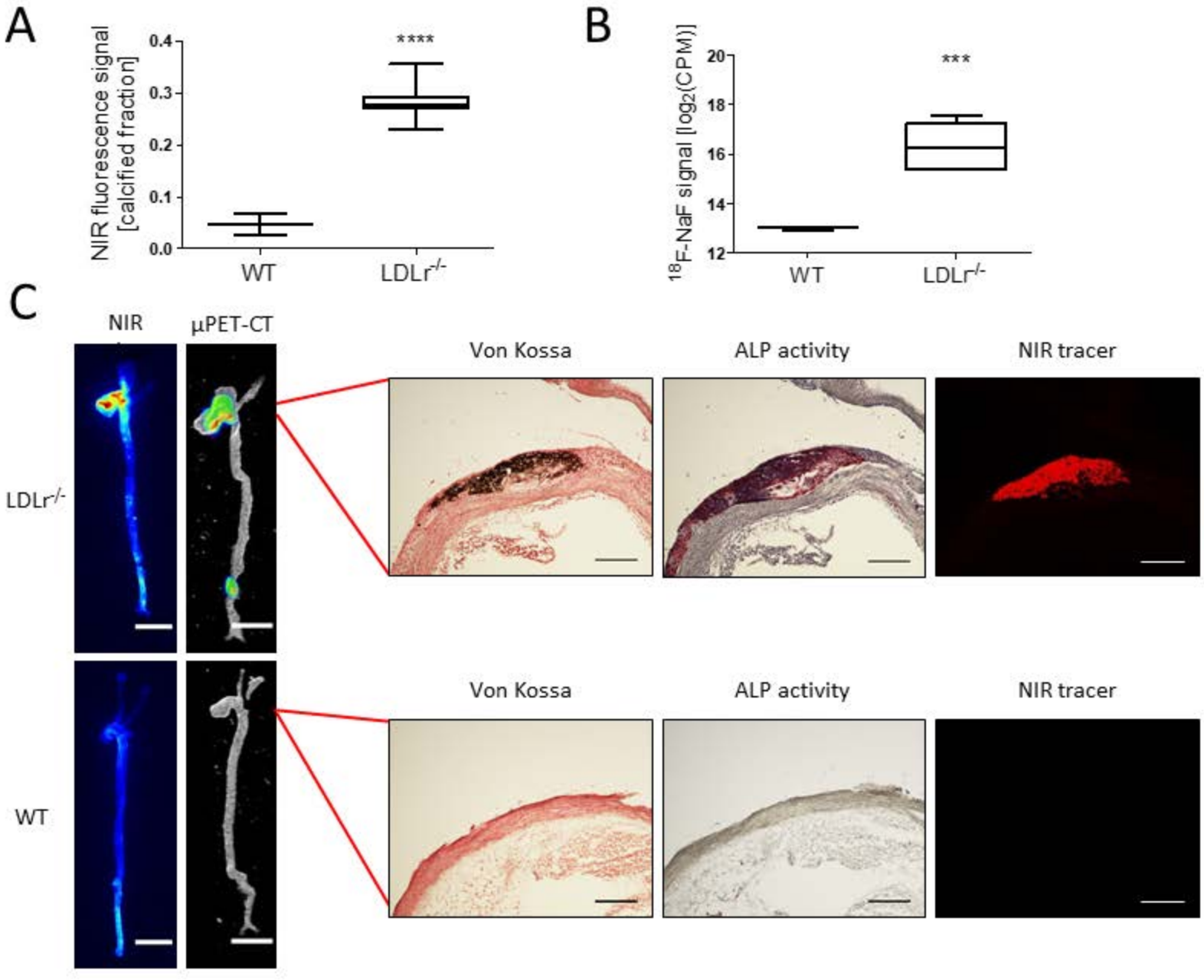
A
NIR fluorescence signal [calcified fraction]
0.4
0.3
0.2
0.1
0.0
****
WT
LDLr-/-
B
18F-NaF signal [log2(CPM)]
20
18
16
14
12
***
WT
LDLr-/-
C
NIR
µPET-CT
LDLr-/-
WT
Von Kossa
ALP activity
NIR tracer
Von Kossa
ALP activity
NIR tracer

SUPPLEMENTAL MATERIAL

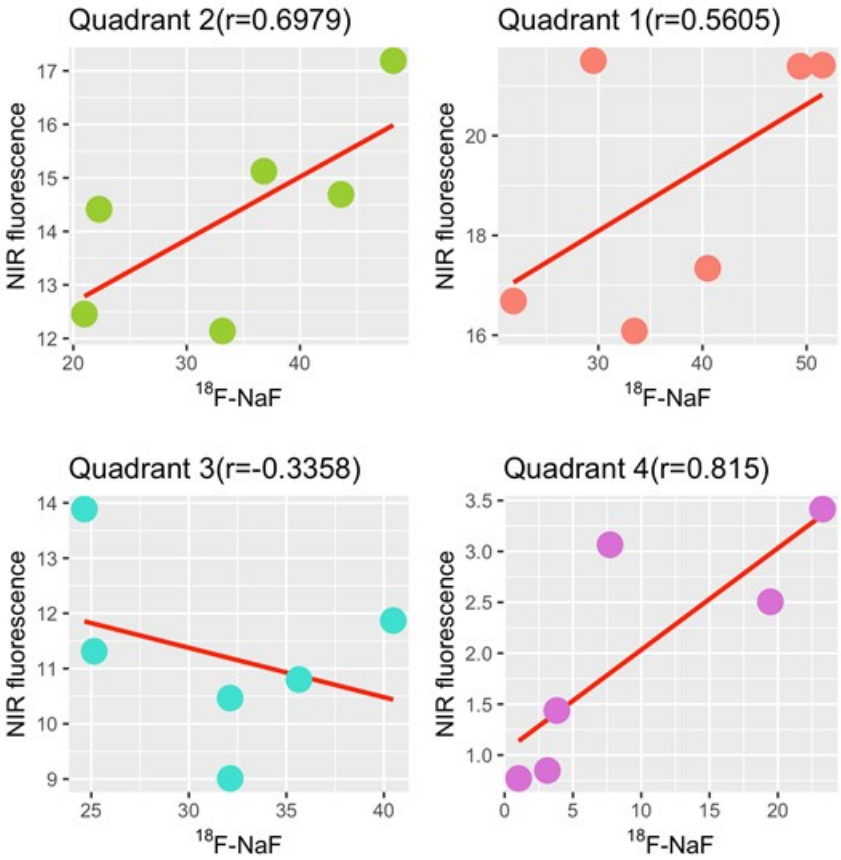

Supplemental Figure 1. Linear correlations within quadrants obtained from sections (Pearson R for Q1=0.5605, Q2=0.6979, Q3=-0.3358 and Q4=0.8150). We found that variance in the model is attributed to random errors from the four image quadrants (87.58% of total variance, Supplementary Table 1). Therefore, we calculated Pearson's R within the four quadrants, respectively (Fig. 4F). Quadrant 3 (Q3) shows a negative correlation, while the other quadrants show positive correlations between the signals. We speculated that histological section 6 (S6) is an outlier causing a negative correlation (Fig. 4F). We conducted Jackknife resampling and calculated Pearson's R to test if S6 is an outlier in Q3 (Supplementary Table 2). The resampled correlation coefficients without S6 (r = -0.3798 ~ 0.8611) are much higher than ones with S6 (r = -0.6819 ~ -0.3141), indicating that S6 is an influential outlier causing a negative correlation in Q3. These findings demonstrate the presence of microcalcifications in areas identified as PET-positive and CT-negative during *ex vivo* PET/CT imaging of explanted specimens.

Supplemental Table 1. Variance component analysis results. We conducted variance component analysis (VCA) for a mixed model for a correlational analysis between NIRF signal and ^{18}F-fluoride autoradiography signal. CV: Coefficient of variation.

	Variance component	Percent to total (%)	CV (%)
Total	23.3549	100	41.449
Quadrant	20.4531	87.5753	38.7886
Histological Sections	1.5833	6.7792	10.792
Error	1.3185	5.6455	9.8484

Supplemental Table 2. Pearson's R in quadrants with Jackknife resampling. We conducted Jackknife resampling for all six sections with or without section 6 (S6) in quadrant 3 and calculated Pearson's r for signals between NIRF and 18F-fluoride. S6: Histological section 6.

Quadrant	Excluded section	Pearson's r with S6	Pearson's r without S6
3	1	-0.4208	0.3239
3	2	-0.6819	-0.3798
3	3	-0.3786	0.8611
3	4	-0.3141	0.2372
3	5	-0.3372	0.2348